International Journal of Thermophysics (2022) 43:37
https://doi.org/10.1007/s10765-021-02969-9

Evaluation of the Effect of Different Nano-Size of WO_3 Addition on the Thermal Properties of HDPE Composite

Amro Obeid[1,2] · Mohamad Roumie[2] · Mohamed. S. Badawi[1] · Ramadan Awad[1,3]

Received: 8 November 2021 / Accepted: 18 December 2021 / Published online: 10 January 2022
© The Author(s), under exclusive licence to Springer Science+Business Media, LLC, part of Springer Nature 2021

Abstract

High-density polyethylene (HDPE) composite has been synthesized with promising characteristics. WO_3 of different particle sizes were obtained through a high speed ball milling techniques at different milling times (15 min, 30 min, 60 min, and 120 min). The resulted particle size was identified using X-ray diffraction and transmission electron microscope and was found to be decreased with the increase of milling time. Bulk micro-sized WO_3 (Sample A) and two selected WO_3 nanoparticles 45 nm (Sample B) and 24 nm (Sample C) were characterized by scanning electron microscope, energy dispersive X-ray and Fourier transform infrared spectroscopy. Various amounts (10 mass%, 15 mass%, 25 mass%, and 35 mass%) of filler (Samples A, B, and C) were incorporated within HDPE and prepared via compression molding technique. The effect of particle size and mass fraction of the thermal properties of the composite was evaluated using thermogravimetric analysis and differential scanning calorimeter (DSC). The results indicated that the addition of WO_3 particles altered the thermal stability and crystallinity, while did not affect the melting temperature HDPE composites. The incorporation of either nano-sized particles WO_3 NPs(B) or (C) up to 25 mass% enhanced the thermal stability of the composites. With respect to pure HDPE, DSC results indicated that the degree of crystallinity increased by the incorporation of WO_3 filler due to the nucleation of HDPE. This improvement in the thermal properties of the nanocomposites suggests promising applications in radiation shielding and industry such as coating, barriers, catalysis, photo corrosion, and photothermal conversion.

Keywords DSC · HDPE composites · TGA · WO_3 nanoparticles

✉ Amro Obeid
amrobeid@gmail.com; a.obeid@cnrs.edu.lb

[1] Department of Physics, Faculty of Science, Beirut Arab University, Beirut, Lebanon

[2] Lebanese Atomic Energy Commission, National Council for Scientific Research, Beirut, Lebanon

[3] Physics Department, Faculty of Science, Alexandria University, Alexandria, Egypt

1 Introduction

The inspiring revolution in materials science and engineering stimulated researchers towards synthesizing and developing new composite materials for practical applications [1–3]. Among the most valuable and interesting materials, polymer nanocomposites are considered to be an advanced alternative composite in terms of their functionality, durability, and easy processing [4]. The enhancement of the properties of polymer nanocomposites is a big challenge since many factors contribute to this procedure such as filler type, filler loading [5], filler dispersion, and adhesion to polymer matrix [6]. Also, the size and morphology of the nanoparticles have a great effect on the composition and structure of the composite [7]. Besides, the preparation conditions play an important role in ameliorating the properties of synthesized composites.

High-density polyethylene (HDPE) [8] is a widely consumed thermoplastic polymer due to its unique characteristics, durability, sustainability, and easy processing. However, many limitations govern the use of HDPE such as restricted thermal stability and structure. The introduction of inorganic filler into the polymer matrix significantly enhances the properties and functionality of the polymer. Among these fillers, tungsten oxide WO_3 was chosen due to its proficient characteristics [9, 10]. WO_3 consists of perovskite units, it is a unique multifunctional material that attracted considerable attention including many fields of research such as thermo- pyroelectricity, water evaporation, near-infrared rays (NIR) shielding, water splitting [11, 12], and gas sensing [13]. Also, tungsten showed excellent stability at higher temperatures, low sputtering yield, and low thermal expansion rate [14]. So, it is quite interesting to add the tungsten-based element to polymers to facilitate its use in harsh environments [15]. Many studies focused on the impact of adding metal oxides, especially WO_3 nanoparticles (NPs) in enhancing the properties of the synthesized composites. Oh *et al*. [16] used in situ metallocene polymerization method to prepare HDPE/WO_3 composites. They determined that HDPE/WO_3 composites had been submitted to heterogeneous nucleation through WO_3 nanoparticles encapsulation.

The crystallization rate was accelerated via the addition of WO_3 nanoparticles by shifting crystallization peaks to higher temperatures. Ambika *et al*. [17] studied the influence of adding various amounts of WO_3 filler particles on the thermal properties of Isophthalic polyester. They found that the sample of 50 mass % WO_3 content exhibited excellent thermal stability. Alsayed *et al*. [18] prepared HDPE/ZnO composite via compression molding technique by adding zinc oxide as a filler (bulk ZnO and ZnO NPs) with a different mass % (0, 10, 20, 30, and 40) to HDPE. The thermal stability of the prepared composite was improved after the incorporation of ZnO filler. Machado *et al*. [19] studied the influence of adding 5 mass% and 10 mass% of WO_3 nanoparticles prepared by solvent casting into poly(ε-caprolactone) (PCL). The results showed that the incorporation of WO_3 nanoparticles into the composite enhanced thermal stability and photodegradation efficiency. Sakthivel *et al*. [20] reported the synthesis of WO_3-rGO nanocomposite by chemical method and microwave irradiation. The obtained results showed

that WO_3-rGO nanocomposite has high thermal stability and can be potentially used in photocatalysis. Pavlenko *et al*. [21] prepared thermoplastic polyimide and tungsten oxide (WO_3) of mass % which varied from 0 mass% to 80 mass% and modified with hydrophobic silicone fluid. The obtained results revealed that the density increased with the addition of filler as well as the heat resistance of polyimide, whereas; the rate of mass loss decreases especially for high filler loading.

Few studies were conducted on the synthesis of HDPE composite by adding different filler sizes of WO_3 at various mass fractions. However, several systematic reviews have reported the influence of particle size and particle loading on the thermal properties of the composites in addition to its ability to develop the radiation attenuation of the composite [22] since the prepared samples will be tested later as radiation shielding materials. This work aims to investigate the effect of 10 mass%, 15 mass%, 25 mass%, and 35 mass% of different particle sizes of WO_3 Bulk(A), NPs(B), and NPs(C) as filler on the thermal and crystallinity behavior of HDPE. In this regard, the new category of HDPE/WO_3 polymer composite with different filler sizes and mass fractions provides useful information for developing the composite properties to effectively withstand harsh environments for further applications in many fields such as research and industry including barriers, radiation shields, coating, catalysis, and photothermal conversion.

2 Experimental Techniques

2.1 Materials

Commercial HDPE (Egyptene HD5403EA grade) supplied by SIDPEC (Sidi-Kerir Petrochemicals Company, Egypt), with density 0.955 $g \cdot cm^{-3}$ and a melt flow index (MFI) of about 0.35 g/10 min was used as a polymer matrix. Tungsten (VI) oxide (WO_3) in powder form with (purity $\geq$ 99%, particle size $\leq$ 25 µm, MW = 231.84 $g \cdot mol^{-1}$, and density = 7.16 $g \cdot cm^{-3}$) was purchased from Sigma Aldrich (USA) and used without further purification.

2.2 WO_3 Nanoparticles Preparation

The mechanical method of a high-energy planetary ball mill (Retsch, PM 100, Germany) in the dry state was used for the preparation of WO_3 NPs. The ball milling process was performed at room temperature in a 250-ml zirconium oxide grinding jar under the following conditions (the ratio of ball to powders mass 10:1, rotation speed about 400 rounds per minute (rpm) and break time = 1 min). Four different milling times were studied, where a specific amount of the bulk micro-sized WO_3 was milled for 15 min and 30 min separately with interval function = 1 min and the same approach was applied for 60 min and 120 min with interval function = 5 min. Four samples of the milled WO_3 at different milling times were characterized and based on the resultant size of NPs achieved, the two milling times at 30 min and 120 min were chosen to give remarkable nano sizes for this study.

2.3 Composite Synthesis

Composites with a filler mass fraction (10 %, 15 %, 25 %, and 35 %) of WO_3 Bulk(A) and WO_3 NPs(B) and WO_3 NPs (C) were prepared using the compression molding technique. Pellets of the HDPE were accurately weighed and poured in a two-roll mill mixer (XK400, Shandong, China) heated at about 170 °C for 15 min and at a speed of 40 rpm. Specific amounts of either WO_3 Bulk(A) or WO_3 NPs (B or C) were added to the mixing chamber after complete melting of the polymer matrix with continuous mixing for 10 min, to prevent their agglomeration. The prepared samples were shaken for 10 min to promote a complete and homogeneous mixing. The samples were gathered, grinded, and molded in a rectangular stainless steel mold of ($25 \times 25 \times 0.3$ cm^3), then layered between Teflon to get a smooth surface. After that, the hot press was applied at 10 MPa and 170 °C for 10 min. Progressively, the pressure was increased to 20 MPa for another 10 min. The shaped composite sample was water-cooled gradually to ambient temperature at the rate (20 °C·min^{-1}). The pure HDPE sample was prepared by a similar method without any WO_3 additive.

3 Characterization Techniques

3.1 XRD Analysis

The X-ray diffraction patterns of bulk WO_3 and the prepared WO_3 nanoparticles samples were obtained by XRD (Bruker, D8 advance, USA) using Cu-k_α radiation source ($\lambda = 0.154$ nm) within a range of $10° \leq 2\theta \leq 70°$. The running conditions for the X-Ray tube were 40 kV and 40 mA, recorded with increment step = 0.02° and exposure time = 1 s. The reference for the peaks fitting was taken from the International Centre for Diffraction Data (ICDD) PDF-2/2013 database.

3.2 TEM Analysis

A transmission electron microscope (JEOL, JEM-2100F, Japan) was used and operated at 200 kV to study the size of the prepared WO_3 nanoparticles. The sample powder was dispersed in ethanol with ultrasonication by directly depositing one drop on a Cu grid.

3.3 SEM and EDX Analysis

Scanning electron microscope and energy dispersive X-ray analysis of WO_3 Bulk(A) and WO_3 NPs(B) and (C) were observed using (JEOL, JCM-6000PLUS, Japan), operated under low vacuum, 15 kV PC-high and magnification order of 1500.

3.4 FTIR Analysis

FTIR analysis was used (Bruker, Vertex 70, USA) to identify the functional groups of WO_3 Bulk(A) and WO_3 NPs(B) and (C). The beam from an IR source passes through a monochromatic controller, ensuring that only specified wavelengths are emitted, with a varying range (2500 cm^{-1} to 400 cm^{-1}). The WO_3 samples are shaped using a hydraulic press and placed in a holder in the path of the IR source.

3.5 Thermogravimetric Analysis (TGA)

TGA of the synthesized composites was performed using (NETZSCH, TG 209F1 Libra, Germany) to investigate the thermal stability of the composites. The selected operation parameters were: 30 °C–600 °C heating range, 10 °C·min^{-1} heating rate in a pure nitrogen atmosphere. The sample mass was taken in the range of 10 mg–15 mg and placed in alumina (Al_2 O_3) crucibles.

3.6 Differential Scanning Calorimeter (DSC)

The DSC of the synthesized composites was measured with (Shimadzu, DSC-60A, Japan) to analyze the melting temperature and crystallinity behavior of the composites. The device was calibrated using the characteristic endothermal peak temperature of a high purity indium standard sample. The analyzed specimens weighing about 3 mg–5 mg were placed in an aluminum pan and tested over the temperature range from room temperature to 200 °C under nitrogen atmosphere, with a scanning rate of 10 °C·min^{-1}.

4 Results and Discussion

4.1 Characterization of WO_3 Particles

The XRD patterns of bulk and milled WO_3 at different milling times (15 min, 30 min, 60 min, and 120 min) have prevailed in Fig. 1. The diffraction peaks displayed nearly the same position with no tangible shift and were found to be highly matched with the ICDD (PDF file 01-083-0951) which indicated the monoclinic structure of WO_3. The main diffraction peaks at 2θ values of 23.118°, 23.583°, 24.365°, 26.592°, 28.614°, 28.979°, 33.262°, 33.564°, and 34.166° correspond to planes (002), (020), (200), (120), (112), (121), (022), (202) and (220). The characteristic peaks of bulk WO_3 indicate high crystallinity due to the strength and sharpness of the peaks. Although the XRD patterns of milled WO_3 showed the same peaks identical to bulk WO_3 with no shift in the position of the peaks. It can be observed a broadening and slight decrease in the peaks intensity as the milling time increased. The sample milled at a time of 120 min showed the lowest and

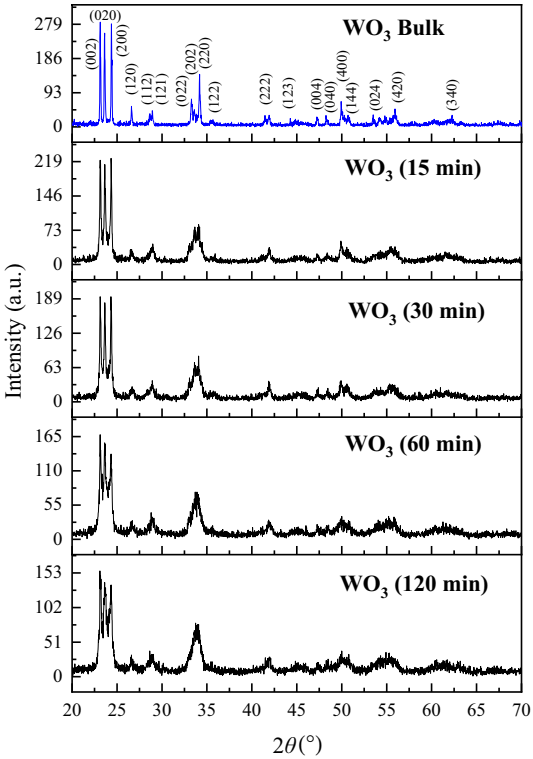

Fig. 1 XRD patterns of WO_3 Bulk micro-sized and WO_3 milled at 15 min, 30 min, 60 min, and 120 min

Table 1 Variation of the broadness of the diffraction peaks and the % crystallinity of bulk and milled WO_3 at different milling times

Sample	FWHM for main characteristic peaks (°)			% Crystallinity
	2Θ = 23.118°	2Θ = 23.583°	2Θ = 24.365°	$\frac{\text{Total area of crystalline peaks}}{\text{Total area of all peaks}}$
Bulk	0.109	0.118	0.115	74.1
15 min	0.125	0.141	0.135	73.8
30 min	0.145	0.183	0.151	69.4
60 min	0.197	0.255	0.198	69.0
120 min	0.216	0.337	0.273	67.5

wide peaks intensity, thus confirming the lowest degree of crystallinity and the smallest crystallite size as shown in Table 1 [23, 24].

The average crystallite size of the milled samples was determined using Scherrer's Eq. 1 and estimated as 69 nm, 45 nm, 32 nm, and 24 nm for the different milling times 15 min, 30 min, 60 min, and 120 min, respectively.

$$D = \frac{0.9\lambda}{\beta \cos\theta} \tag{1}$$

where D, is the mean crystallite size, λ the wavelength of Cu Kα, ($\lambda = 1.5405$ Å), β the full width at half maximum intensity of the peak (FWHM) in radians, and 2θ is Bragg's diffraction angle.

The obtained results of the crystallite size using the mechanical milling process were comparable to other studies using different methods where WO_3 NPs prepared by a flame spray process having a size range between 18 nm and 73 nm [25] and others having a size 54.3 nm prepared by reverse microemulsion (RME) protocol [26] and by a solvothermal method having WO_3 nanoparticles in the 5 nm–30 nm range [27].

Complementary TEM micrographs for the samples of WO_3 milled at different times 15 min, 30 min, 60 min, and 120 min are described in Fig. 2 (a)–(d). The different particle size distribution based on the length scale provided in TEM images was measured using ImageJ software where Gaussian distribution was performed. The average particle size calculated from TEM (Gaussian fitting of size distribution) for milled WO_3 at milling time 15 min, 30 min, 60 min, and 120 min is 74 nm, 50 nm, 36 nm, and 27 nm, respectively. The results are approximately consistent with the average size extracted from XRD patterns of milled WO_3. This convergence in size obtained from TEM and XRD agrees with that reported in previous literature [28–30].

Based on the resultant particle size achieved through the mechanical milling technique, the two milling times at 30 min (45 nm) and 120 min (24 nm) were chosen to give remarkable nano sizes for this study in addition to the bulk WO_3. Therefore, the different particle size of WO_3 used for the composite synthesis was identified as WO_3 Bulk(A) for micro-sized, WO_3 NPs(B) for 45 nm size, and WO_3 NPs(C) for 24 nm size. Figure 3 (a)–(c) show the SEM images and EDX analysis of bulk WO_3 particles, WO_3 NPs (B), and NPs(C). The SEM image of bulk WO_3 particles revealed that WO_3 particles are nearly cubic, whereas WO_3 NPs(C) show the presence of clearly fine aggregates and smaller average particle sizes compared to WO_3 NPs(B). EDX elemental analysis showed peaks confirming the existence of W and O elements as main composed for the three different particle sizes of WO3 samples together with the presence of carbon peaks which could be attributed to the carbon tape used to fix the specimen during the process of spectroscopy. The very weak peak of Al present in the spectrum could be attributed to the specimen pedestal used during the process of spectroscopy. The intensity of the W peak is appeared to be increased to the lowest particle size indicating that WO_3 NPs(C) occupy the largest surface of the quantitative analysis due to the large surface-to-volume ratio of the nanoparticles. Table 2 presents the EDX results of the Mass% distribution of W and O in all investigated WO_3 samples.

The FTIR spectra for the different particle sizes of WO_3 samples Bulk(A), NPs(B), and NPs(C) are shown in Fig. 4, the main tungsten oxide vibrations were observed in the region 500 cm^{-1}–1000 cm^{-1}. For the bulk sample, characteristic peaks at 505.8 cm^{-1} and 832.7 cm^{-1} were detected and referred to (O–W–O) and (W–O) stretching vibrations, respectively [31]. Whereas, these peaks were shifted to (630.3 cm^{-1}–817.8 cm^{-1}) and (625.5 cm^{-1}–819 cm^{-1}) for WO_3 NPs (B) and WO_3 NPs (C), respectively, which confirms that a decrease in the particle size induces a shift to higher wavenumbers. In addition, it is noted that a decrease in the particle size from Bulk to Nanosize implies an

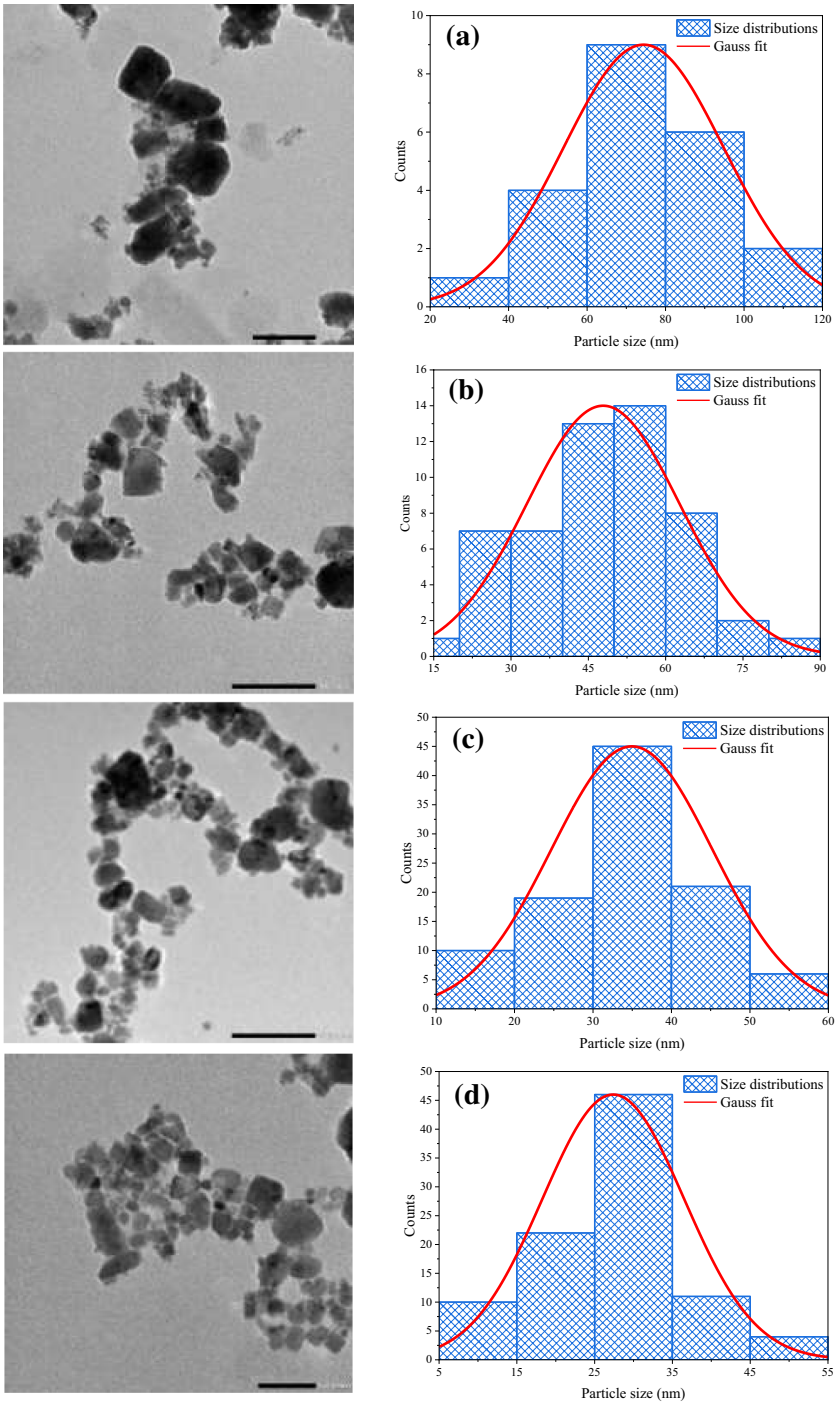

Fig. 2 TEM micrographs and particle size distribution of WO_3 milled at (a) 15 min, (b) 30 min, (c) 60 min, and (d) 120 min

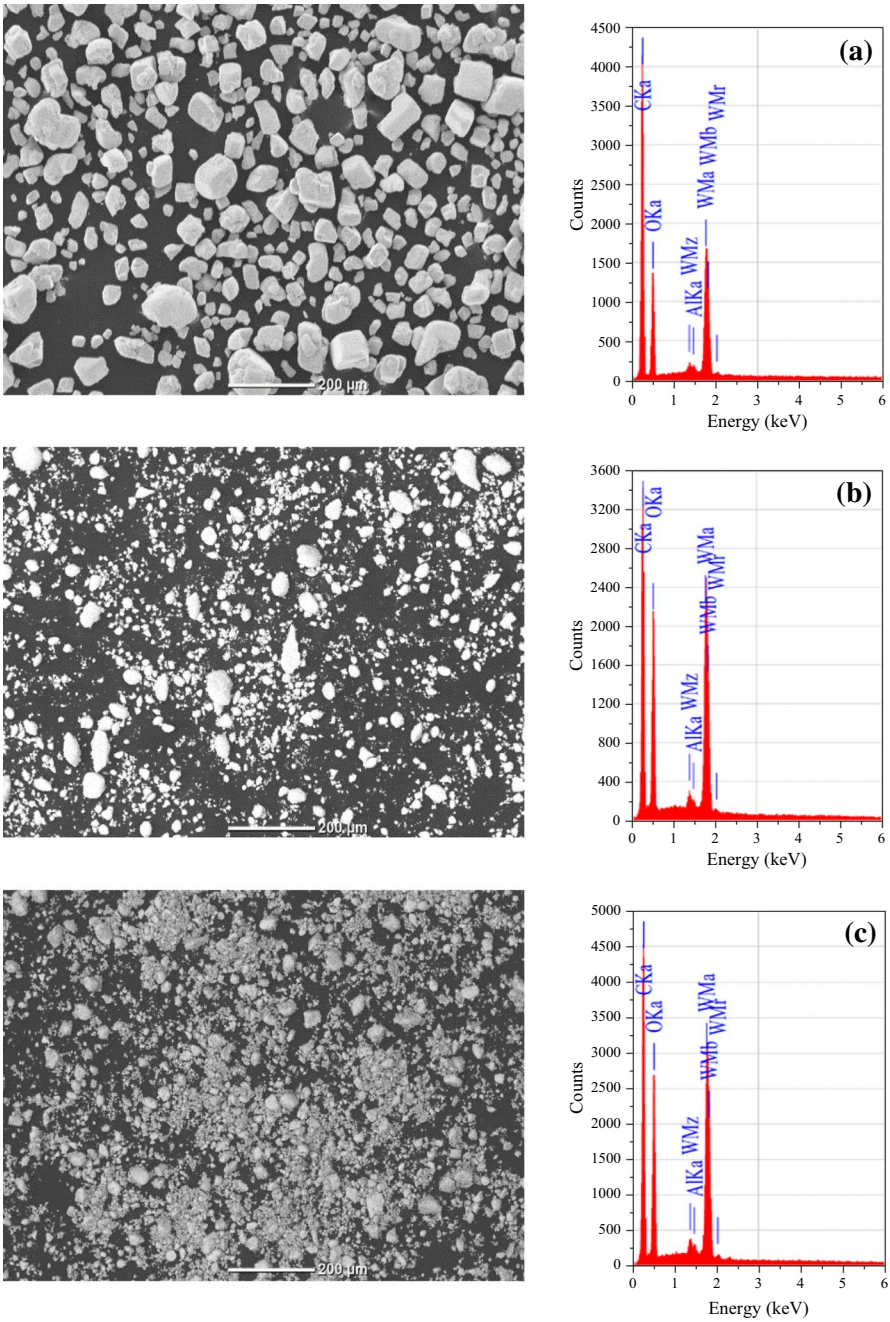

Fig. 3 SEM images and EDX spectrum of (a) WO_3 Bulk (A), (b) WO_3 NPs(B) and (c) WO_3 NPs(C)

Table 2 EDX results of the Mass% distribution of W and O elements in all investigated WO_3 samples

Elements	(keV)	Mass%		
		WO_3 Bulk(A)	WO_3 NPs(B)	WO_3 NPs(C)
W	1.774	22.05	42.88	43.55
O	0.525	21.97	17.82	17.45

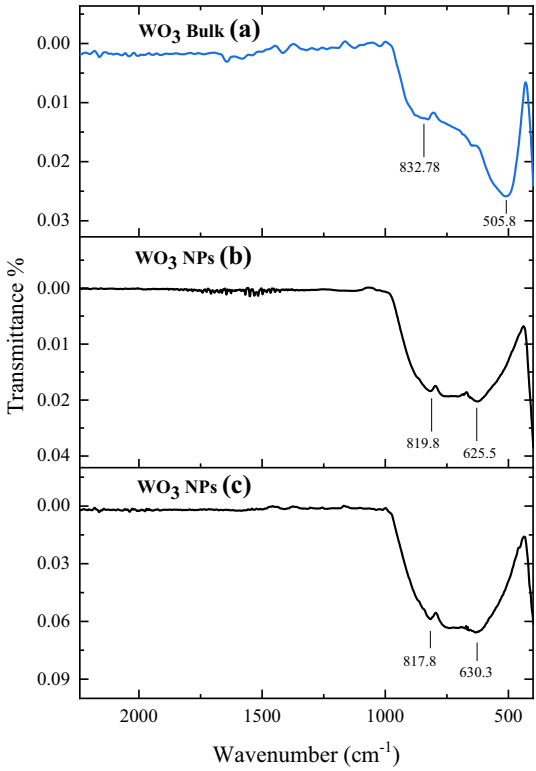

Fig. 4 FTIR spectra of WO_3 Bulk (A), WO_3 NPs (B), and WO_3 NPs

increase in the intensity of characteristic bands the band near 800 shows higher intensities as the particle size diminishes. As mentioned in the literature [32] the particle size affects both the intensity and the width of the emitted peaks in the IR analysis. The obtained characteristic bands of WO_3 NPs(B) and NPs(C) are compatible with that produced by the solvothermal cum chemical reduction route [29, 33] and others prepared by the soft chemical co-precipitation method [34].

4.2 Thermal Properties

4.2.1 TGA

The TGA curves of HDPE and its composites HDPE/WO_3 Bulk(A), HDPE/WO_3 NPs(B), and HDPE/WO_3 NPs(C) are illustrated by Fig. 5 (a)–(c).

Also, the numerical values of the curves are listed in Table 3. T_{ini} is known as the onset thermal decomposition temperature corresponding to 5% mass loss while $T_{50\%}$ corresponds to the temperature where half mass loss of the degradation sample was reached. As shown by Fig. 5, HDPE exhibited mass balance until reaching its initial decomposition temperature at 444 °C [35], where the mass drops dramatically.

The decomposition of HDPE was completed by reaching the final degradation temperature at 503 °C followed by a plateau region, representing approximately a full decomposition at 600 °C with a residual mass of 0.9%. On the other hand, the thermal stability of HDPE was significantly altered with the different filler content. Figure 5 (a) illustrates the TGA curves of HDPE/WO_3 Bulk(A) composites. The curves clearly show a delay in the thermal degradation trajectories at all temperature

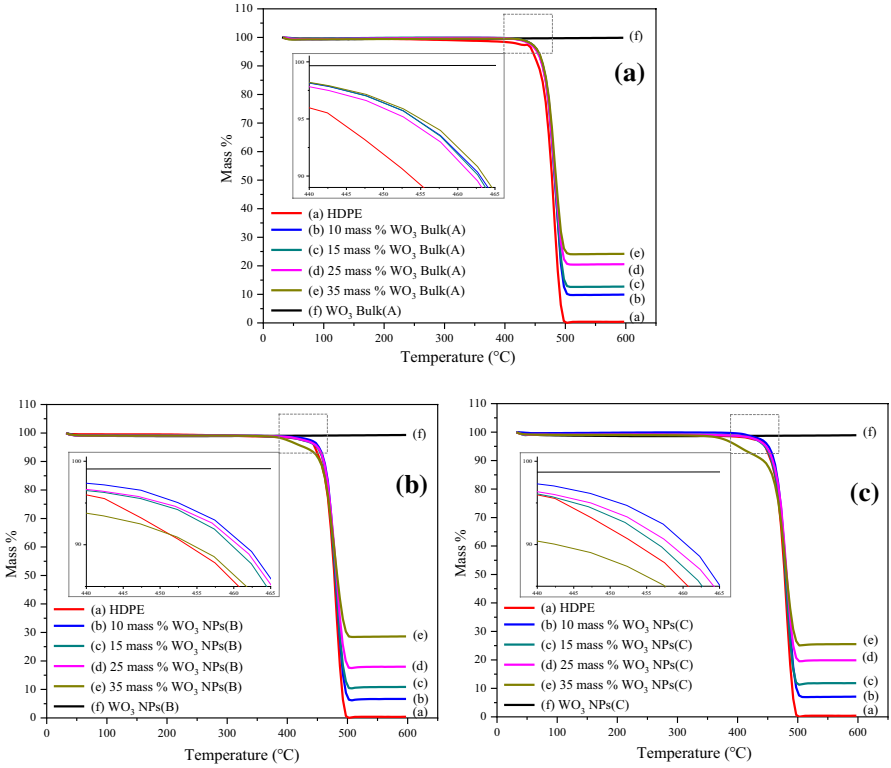

Fig. 5 TGA curves of (a) HDPE/WO_3 Bulk (A) composites, (b) HDPE/WO_3 NPs (B) composites, and (c) HDPE/WO_3 NPs (C) composites

Table 3 TGA degradation temperatures for HDPE, WO_3 Bulk (A), WO_3 NPs (B), WO_3 NPs (C), HDPE/WO_3 bulk (A), HDPE/WO_3 NPs (B), and HDPE/WO_3 NPs (C) composites

Sample	*T* (5%) C	*T* (50%) C	Residual mass%
HDPE	444	478	00.90
WO_3 Bulk(A)	–	–	99.90
10 mass% WO_3 Bulk(A)	455	483	09.89
15 mass% WO_3 Bulk(A)	455	484	12.70
25 mass% WO_3 Bulk(A)	455	484	20.55
35 mass% WO_3 Bulk(A)	456	485	24.17
WO_3 NPs(B)	–	–	99.30
10 mass% WO_3 NPs(B)	453	481	06.95
15 mass% WO_3 NPs(B)	451	481	11.04
25 mass% WO_3 NPs(B)	451	482	19.38
35 mass% WO_3 NPs(B)	429	483	28.62
WO_3 NPs(C)	–	–	98.90
10 mass% WO_3 NPs(C)	452	481	07.08
15 mass% WO_3 NPs(C)	446	481	11.83
25 mass% WO_3 NPs(C)	448	483	19.87
35 mass% WO_3 NPs(C)	401	482	25.53

stages of degradation (T_{ini} and $T_{50\%}$). As listed in Table 3, the samples with 10 mass% and 35 mass% of WO_3 Bulk(A) showed an increase in the values of T_{ini} from 454 °C to 456 °C and $T_{50\%}$ from 483 °C to 485 °C, respectively. Also, the final residual mass at 600 °C for samples with 10 mass% and 35 mass% of WO_3 Bulk(A) increased to 9.89 % and 24.17 %, respectively. The curves in Fig. 5 (b) show a delay in the thermal degradation trajectories at all temperature degradation stages with the incorporation of 10 mass% to 25 mass% WO_3 NPs (B). As listed in Table 3 the 10 mass% and 25 mass% WO_3 NPs (B) filler decreased the values of T_{ini} and increased the values of $T_{50\%}$ from 453 °C, 481 °C to 451 °C, 482 °C, respectively. While the final residual mass at 600 °C increased to 6.95 % and 19.38 %, respectively. However, the addition of 35 mass% WO_3 NPs (B) showed a difference in the TGA curve slope presenting a slow mass decline at the initial degradation stage and then the mass drops dramatically to the final degradation temperature at 600 °C.

The onset degradation temperature T_{ini} of 35 mass% WO_3 NPs (B) exhibited a value preceding to the net HDPE to 429 °C while an increase appeared at the second degradation stage $T_{50\%}$ to 483 °C and the residual mass to 28.62 % as listed in Table 3. it is obvious from Fig. 5 (c) that HDPE/WO_3 NPs(C) composites showed similar behavior of thermal degradation trajectories but with fewer values of the initial degradation temperature compared to HDPE incorporated with WO_3 NPs(B) at the same mass % filler. As listed in Table 3, the 10 mass% and 25 mass% of WO_3 NPs(C) samples showed a drop in the values of T_{ini} from 452 °C to 448 °C and a rise in the values of $T_{50\%}$ from 481 °C to 482 °C. While the final residual mass at 600 °C increased to 7.08 % and 19.87 %. Besides, HDPE with 35 mass% of WO_3 NPs(C) showed an obvious difference in the TGA curve slope at the initial degradation stage steeper compared to that incorporated with the same filler content of WO_3 NPs(B), the values of T_{ini} decreased to 401 °C and the final residual mass at 600 °C increased

to 25.53 %. As deduced from Fig. 5 and Table 3, WO_3 Bulk, WO_3 NPs(B), and WO_3 NPs(C) exhibited high thermal stability up to 600 °C with only 0.1 %, 0.7 %, and 1.1 % total mass loss, respectively, indicating the existence of moisture observed in smaller size WO_3 NPs(C) [36].

It can be concluded that the increment in the filler content for both WO_3 NPs(B) and NPs(C) to 35 mass% inhibited the thermal stability of the composite at the early stages of the degradation by shifting T_{ini} to lower values while maintaining thermal stability until reaching the final degradation temperature. Due to the adsorption of the fillers on the surface of the polymer matrix, NPs tend to agglomerate. Besides, the presence of cracks at high filler loading was revealed by SEM which in turn affects the role of filler NPs as a barrier towards the diffusion of oxygen and volatile degradation products. The factors influencing the thermal stability of the polymer composites depend on the degree and type of dispersion of the reinforcing agent in the host matrix, their interfacial adhesion, specimen geometry environmental, oxygen concentration, and moisture content [37].

4.2.2 DSC

The DSC heating thermograms for HDPE and its composites are demonstrated in Fig. 6. The crystalline melting temperature is shown as an endothermal peak. The

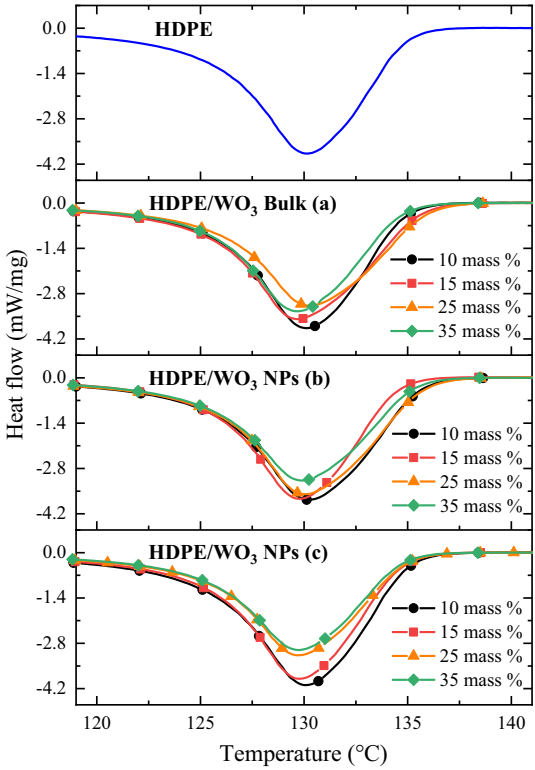

Fig. 6 DSC for HDPE and its WO_3 Bulk(A), WO_3 NPs(B), and WO_3 NPs(C) composites

Table 4 DSC degradation for HDPE, HDPE/WO_3 bulk (A), HDPE/WO_3 NPs (B), and HDPE/WO_3 NPs (C) composites

Sample	Endothermal				
	T_{onset}	T_m	T_{endset}	ΔH ($J \cdot g^{-1}$)	X_c (%)
HDPE	126	130	135	− 158.52	54.10
10 mass% WO_3 Bulk(A)	126	130	135	− 155.13	58.75
15 mass% WO_3 Bulk(A)	126	130	136	− 147.27	57.57
25 mass% WO_3 Bulk(A)	126	130	136	− 124.05	54.14
35 mass% WO_3 Bulk(A)	126	130	135	− 121.42	54.64
10 mass% WO_3 NPs(B)	126	130	136	− 151.13	55.43
15 mass% WO_3 NPs(B)	125	130	134	− 150.81	57.85
25 mass% WO3 NPs(B)	126	130	136	− 141.17	59.76
35 mass% WO_3 NPs(B)	125	130	135	− 139.21	66.56
10 mass% WO_3 NPs(C)	126	130	135	− 174.67	64.15
15 mass% WO_3 NPs(C)	125	130	135	− 159.45	61.72
25 mass% WO_3 NPs(C)	126	130	135	− 134.16	57.14
35 mass% WO_3 NPs(C)	125	130	135	− 125.90	57.70

degree of crystallinity was determined by Eq. 2 assuming that the presence of WO_3 does not affect the crystallization mechanism of HDPE. The heat of fusion was calculated by the integration of the endothermal peak area in the evaluated temperature range.

$$X_C = \frac{\mathbf{\Delta}\mathrm{H}}{(\mathbf{1}-\mathrm{W_a})\mathbf{\Delta}\mathrm{H_0}} \times 100\%, \tag{2}$$

where X_C is crystallinity of semi-crystalline polymer, ΔH is the heat of fusion of semi-crystalline polymer and its composites, W_a is the actual mass fraction of WO_3 filler, and ΔH_0 is the heat of fusion of 100% crystalline polyethylene ($\Delta H_0 = 293$ [$J \cdot g^{-1}$] [38]).

The results of DSC measurement: The onset, peak, endset melting temperature, the heat of fusion, and the % crystallinity are determined and listed in Table 4. There is no considerable change in the characteristic endothermal peak temperature T_{onset}, $T_{m,}$ and T_{endset} which recorded a value near 126 °C, 130 °C, and 135 °C for all HDPE composites, while the heat of fusion of the composites decreases with increasing the composite filler content. This may be due to the inhibition of close packing corresponding to HDPE chains as WO_3 particles are physically dispersed in the polymer matrix. The observed behaviors of the characteristic endothermal peak temperature, and the heat of fusion are similar to that reported by Rajeshwari et al. for HDPE/n-AlN polymer composites [35] and Mosavian *et al.* for HDPE/Al_2O_3 polymer composites [39].

As can be seen from Table 4, the values of X_C % of the composites increase by adding various mass fraction of WO_3 filler as compared to the pure polymer matrix. Also, the values of X_c % slightly decrease and stabilize for the high mass fraction 25 mass% and 35 mass% with the exception of HDPE/WO_3 NPs(C),

which exhibited an increase in X_c % as the mass fraction increases. These results indicate a good dispersion of the filler in the polymer matrix even in the amorphous region of HDPE, in addition to its ability to induce the nucleation of HDPE [40]. The melting-recrystallization-remelting mechanism proposes that original imperfect thin crystals or lamellae in the polymers could melt and recrystallize to form crystals of higher perfection during DSC scans, according to the result reported by Kim *et al*. [41] in their study.

5 Conclusion

The results indicated a monoclinic phase for WO_3 particles and exhibited a change in the crystallite size between the different milling times of WO_3 particles. The average sizes of the milled WO_3 particles recorded by TEM were consistent with XRD results. SEM/EDX analysis for WO_3 bulk(A), WO_3 NPs(B), and (C) revealed the existence of W and O elements and showed an increase in the intensity of W peak to the lowest particle size, indicating the large surface-to-volume ratio of the nanoparticles. The FTIR results showed a shift of the stretching vibrational mode near 500 cm^{-1} for WO_3 bulk(A) to higher wavenumbers near 600 cm^{-1} for both WO_3 NPs(B) and NPs(C). Furthermore, the different sizes and mass fractions of WO_3 nanoparticles showed a significant effect on the thermal properties of the HDPE composites. The TGA data clarified that the incorporation of both WO_3 NPs(B) and (C) up to 25 mass % improved the thermal stability of the composite. With respect to pure HDPE, the DSC heating thermograms measurements showed a decrease in heats of fusion in all tested samples with increasing filler loading while the ability to induce the nucleation of HDPE was appeared by increasing the degree of crystallinity. Besides, no considerable changes were detected in the melting temperature of the HDPE composites at all WO_3 filler loading. Based on the results, it is deduced that the agglomeration of WO_3 nanoparticles at high filler loading affected the properties of composites due to the filler adsorption on the surface of the polymer matrix, therefore, a fine dispersion of the nanofiller is needed by controlling some process parameters during compression molding technique such as: extending the agitation time in the mixer chamber to improve the homogeneity of the fillers in the polymer matrix, and reducing the water cooling rate of the shaped composite samples under the hot press to prevent the formation of cracks and voids.

Acknowledgments This work was done in the frame of the scientific collaboration between the Physics Department, Faculty of Science, Beirut Arab University (BAU), and the National Council for Scientific Research-Lebanon (CNRSL), Lebanese Atomic Energy Commission (LAEC). The main author would like to thank Dr. Malek Tabbal, Professor of Physics at the American University of Beirut (AUB), and the Lab's Staff at KAS CRSL-AUB, for XRD and TGA measurements and their valuable support.

Declarations

Conflict of interest The authors declare that they have no competing interest.

References

1. P. Shukla, P. Saxena, Chin. J. Polym. Sci. **39**, 665 (2021). https://doi.org/10.1007/s10118-021-2553-8
2. M. Nasirinezhad, S.R. Ghaffarian, M. Tohidian, Iran. Polym. J. **30**, 355 (2021). https://doi.org/10.1007/s13726-020-00895-5
3. S.S. Azari, A. Alizadeh, L. Roufegarinejad, N. Asefi, H. Hamishehkar, J. Polym. Environ. **29**, 1143 (2021). https://doi.org/10.1007/s10924-020-01950-1
4. T. Hassan, A. Salam, A. Khan, S.U. Khan, H. Khanzada, M. Wasim, M.K. Khan, J. Polym. Res. **28**, 36 (2021). https://doi.org/10.1007/s10965-021-02408-1
5. S. Murugan, P.R. Thyla, N. Mahendrakumar, K.N. Manojkumar, A. Siddarth, Iran. Polym. J. **30**, 93 (2021). https://doi.org/10.1007/s13726-020-00876-8
6. J.F. Vega, Y. da Silva, E. Vicente-Alique, R. Núñez-Ramírez, M. Trujillo, M.L. Arnal, A.J. Müller, P. Dubois, J. Martínez-Salazar, Macromolecules **47**, 5668 (2014). https://doi.org/10.1021/ma501269g
7. G.I. Dzhardimalieva, I.E. Uflyand, J. Polym. Res. **25**, 255 (2018). https://doi.org/10.1007/s10965-018-1646-8
8. S. Sánchez-Valdes, Iran. Polym. J. **30**, 297 (2021). https://doi.org/10.1007/s13726-020-00889-3
9. J. Gupta, H. Shaik, K.N. Kumar, Ionics **27**, 2307 (2021). https://doi.org/10.1007/s11581-021-04035-8
10. M. Ikram, M.M. Sajid, Y. Javed, A.M. Afzal, N.A. Shad, M. Sajid, K. Akhtar, M.I. Yousaf, S.K. Sharma, H. Aslam, T. Hussain, D. Hussain, A. Razaq, J. Mater. Sci. Mater. Electron. **32**, 6344 (2021). https://doi.org/10.1007/s10854-021-05351-5
11. C.M. Wu, S. Naseem, M.H. Chou, J.H. Wang, Y.Q. Jian, Front. Mater. **6**, 49 (2019). https://doi.org/10.3389/fmats.2019.00049
12. Y. Shabdan, A. Markhabayeva, N. Bakranov, N. Nuraje, Nanomaterials **10**, 1871 (2020). https://doi.org/10.3390/nano10091871
13. Z. Wei, Q. Zhou, W. Zeng, Nanotechnology **31**, 215701 (2020). https://doi.org/10.1088/1361-6528/ab73bd
14. K.J. Kim, M.S. Park, Y.J. Kim, J.H. Kim, S.X. Dou, M. Skyllas-Kazacos, J. Mater. Chem. A **3**, 16913 (2015). https://doi.org/10.1039/C5TA02613J
15. L. Singheiser, T. Hirai, J. Linke, G. Pintsuk, M. Rödig, Trans. Indian Inst. Met. **62**, 123 (2009). https://doi.org/10.1007/s12666-009-0016-y
16. K. Oh, W.H. Chua, S.E. Park, J. Kim, S. Kwak, S. Kim, Y. Seo, Macromol. Res. **23**, 265 (2015). https://doi.org/10.1007/s13233-015-3041-1
17. M.R. Ambika, N. Nagaiah, K. Prashantha, Int. J. Polym. Anal. Chem. **25**, 431 (2020). https://doi.org/10.1080/1023666X.2020.1803566
18. Z. Alsayed, R. Awad, M.S. Badawi, Iran. Polym. J. **29**, 309 (2020). https://doi.org/10.1007/s13726-020-00796-7
19. A.V. Machado, G. Botelho, M.M. Silva, I.C. Neves, A.M. Fonseca, J. Polym. Res. **18**, 1743 (2011). https://doi.org/10.1007/s10965-011-9580-z
20. T. Sakthivel, E. Manikandan, V. Gunasekaran, Mater. Express **2**, 327 (2012). https://doi.org/10.1166/mex.2012.1087
21. V.I. Pavlenko, G.G. Bondarenko, N.I. Cherkashina, Inorg. Mater. Appl. Res. **11**, 304 (2020). https://doi.org/10.1134/S2075113320020306
22. C.V. More, Z. Alsayed, M.S. Badawi, A.A. Thabet, P.P. Pawar, Environ. Chem. Lett. **19**, 2057 (2021). https://doi.org/10.1007/s10311-021-01189-9
23. V. Shakya, N.K. Pandey, S.K. Misra, A. Roy, Bull. Mater. Sci. **40**, 253 (2017). https://doi.org/10.1007/s12034-017-1373-5
24. S.R. Chandra, M. Hegde, C.N.R. Rao, Sens. Actuators B Chem. **128**, 488 (2008). https://doi.org/10.1016/j.snb.2007.07.013
25. D. Hidayat, A. Purwanto, W.N. Wang, K. Okuyama, Mater. Res. Bull. **45**, 165 (2010). https://doi.org/10.1016/j.materresbull.2009.09.025
26. S. Zhang, D.F. Consoli, S.K. Shaikh, Y. Roman-Leshkov, Appl. Catal. A **580**, 53 (2019). https://doi.org/10.1016/j.apcata.2019.04.019
27. N. Le Houx, G. Pourroy, F. Camerel, M. Comet, D. Spitzer, J. Phys. Chem. C **114**, 155 (2009). https://doi.org/10.1021/jp908669u

28. H.H. Afify, S.A. Hassan, M. Obaida, I. Moussa, A. Abouelsayed, Opt. Laser Technol. **111**, 604 (2019). https://doi.org/10.1016/j.optlastec.2018.10.036
29. V.B. Kumar, D. Mohanta, Bull. Mater. Sci. **34**, 435 (2011). https://doi.org/10.1007/s12034-011-0117-1
30. M. Bourdin, M. Gaudon, F. Weill, M. Duttine, M. Gayot, Y. Messaddeq, T. Cardinal, Nanomaterials **9**, 1555 (2019). https://doi.org/10.3390/nano9111555
31. B. Ingham, S.V. Chong, J.L. Tallon, J. Phys. Chem. B **109**, 4936 (2005). https://doi.org/10.1021/jp045066l
32. B. Udvardi, I.J. Kovács, T. Fancsik, P. Kónya, M. Bátori, F. Stercel, G. Falus, Z. Szalai, Appl. Spectrosc. **71**, 1157 (2017). https://doi.org/10.1177/0003702816670914
33. I. Aslam, M.H. Farooq, M.W. Iqbal, R. Boddula, M. Abid, M. Ashfaq, U. Ghani, Mater. Sci. Energy Technol. **2**, 187 (2019). https://doi.org/10.1016/j.mset.2019.02.002
34. S. Azmat, T. Jan, S.Z. Ilyas, A. Hassan, I. Habib, Q. Mahmood, A. Mahmood, Mater. Res. Express **5**, 115025 (2018). https://doi.org/10.1088/2053-1591/aadf0a
35. P. Rajeshwari, T.K. Dey, J. Therm. Anal. Calorim. **118**, 1513 (2014). https://doi.org/10.1007/s10973-014-4063-1
36. J.S. Neves, F. Machado, F.G. de Souza Jr, P.A.Z. Suarez, A.P. Umpierre, Macromol. Mater. Eng. **296**, 1107 (2011). https://doi.org/10.1002/mame.201100050
37. M. Kutz, *Handbook of Environmental Degradation of Materials*, 2nd edn. (Elsevier, Amsterdam, 2012)
38. M. Saleh, Z. Al-Hajri, A. Popelka, S.J. Zaidi, Materials **13**, 250 (2020). https://doi.org/10.3390/ma13010250
39. M.T.H. Mosavian, A. Bakhtiari, S. Sahebian, Polym. Plast. Technol. Eng. **51**, 214 (2012). https://doi.org/10.1080/03602559.2011.557820
40. A. Diop, F. Mijiyawa, D. Koffi, B.V. Kokta, D. Montplaisir, J. Thermoplast. Compos. Mater. **28**, 1662 (2015). https://doi.org/10.1177/0892705714556829
41. J.Y. Kim, S.H. Kim, S.W. Kang, J.H. Chang, S.H. Ahn, Macromol. Res. **14**, 146 (2006). https://doi.org/10.1007/BF03218502

Publisher's Note Springer Nature remains neutral with regard to jurisdictional claims in published maps and institutional affiliations.